Characterization of Environmental Seismic Signals in a Post-Wildfire Environment: Examples from the Museum Fire, AZ

Ryan Porter[1], Taylor Joyal[1], Rebecca Beers[2], Ann Youberg[2], Joseph Loverich[3], Edward Schenk[4], Peter R. Robichaud[5]

[1]School of Earth and Sustainability, Northern Arizona University, Flagstaff, AZ, United States

[2]Arizona Geological Survey, University of Arizona, Tucson, AZ, United States

[3]JE Fuller Hydrology and Geomorphology, Inc., Flagstaff, AZ, United States

[4]Flagstaff Water Services, City of Flagstaff, Flagstaff, AZ, United States

[5]US Department of Agriculture, Forest Service, Rocky Mountain Research Station, Moscow, ID, United States

Corresponding author: Ryan Porter (ryan.porter@nau.edu)

Key Points:

- Seismic monitoring of debris flows is effective in post-wildfire environments
- Rainfall, wind, and lightning can be detected and characterized with seismic data
- Existing theoretical work provides important context for understanding debris flows in post-wildfire settings

Abstract

The 2019 Museum Fire burned in a mountainous region near the city of Flagstaff, AZ, USA. Due to the high risk of post-wildfire debris flows and flooding entering the city, we deployed a network of seismometers within the burn area and downstream drainages to examine the efficacy of seismic monitoring for post-fire flows. Seismic instruments were deployed during the 2019, 2020, and 2021 monsoon seasons following the fire and recorded several debris flow and flood events, as well as signals associated with rainfall, lighting and wind. Signal power, frequency content, and wave polarization were measured for multiple events and compared to rain gauge records and images recorded by cameras installed in the study area. We use these data to demonstrate the efficacy of seismic recordings to (1) detect and differentiate between different energy sources, and (2) estimate the timing of lightning strikes, rainfall intensity, and debris flow timing, size, velocity, and location. This work confirms the validity of theoretical models for interpreting seismic signals associated with debris flows and rainfall in post-wildfire settings and demonstrates the efficacy of seismic data for identifying and characterizing debris flows.

Plain Language Summary

Wildfires are a growing hazard as the size and frequency of high-severity fires are growing globally. Following containment, post-fire flooding and debris flows can put downstream communities at risk, particularly as communities expand within the wildland-urban interface and close to fire-prone mountains. In this work, we use seismic instruments to measure ground vibrations created by rainfall, lightning, debris flows and floods as they move downstream and compare these recordings to game camera photos and rainfall records. This dataset allows us to detect and better understand hazards in post-wildfire areas. Observations

from these instruments show a high potential for detecting these events and the validity of using seismic data as a tool for understanding debris flow behavior.

1 Introduction

1.1 Wildfires are a growing risk globally as the size, and frequency of high severity events are increasing due to climate change (Abatzoglou & Williams, 2016; Jolly et al., 2015; Westerling, 2016; Westerling et al., 2006). In the western US, wildfire risk is particularly acute as a century of excessive fire suppression has resulted in high fuel loads in many forests, which, when combined with climate change effects, has led to several catastrophic fires in recent years (Parks et al., 2015; Steel et al., 2015). Further, wildfires are becoming an increasing threat to people, property, and infrastructure as communities expand into the wildland-urban interface (Radeloff et al., 2018). Beyond the threat of wildfires themselves, post-fire debris flows and floods present a risk to downstream communities that can persist for years following fire containment. In this work, we present an analysis of seismic data recorded during post-fire debris flow and flood events emanating from the 2019 Museum Fire scar. This fire and the landscape's post-fire response are characteristic of what we may expect following future wildfires within the southwestern United States (Sankey et al., 2017). We use these data to demonstrate the efficacy of using seismic instruments and analysis techniques to detect and characterize post-fire debris flows and flooding. We compare our observations to debris-flow seismic models in order to provide a framework for future work using seismic data in post-fire settings.

1.2 The Museum Fire, located in the Dry Lake Hills and Mount Elden immediately north of Flagstaff, AZ (Figure 1) ignited July 21, 2019 during an abnormally dry monsoon season due to a rock strike by heavy equipment during forest thinning activities (Museum Fire BAER Team, 2019). The fire occurred in ponderosa pine (*Pinus ponderosa*) and mixed conifer forest at

elevations between ~2200 and ~2750 m. Full containment was achieved on August 12, 2019 with an estimated burned area of ~8 km^2. Post-fire assessment of the burn area estimated that 12% of the soil burn severity was very low, 48% was low, 28% was moderate, and 12% was high (Figure 2; Museum Fire BAER Team, 2019). Most of the burn area drains into the Spruce Wash Watershed (SWW), an ephemeral drainage that flows through communities in eastern Flagstaff. The watershed is located on mountainous terrain comprised of Pleistocene-age dacitic lava domes with steep flanks (Holm, 1988; Figure 1). The watershed is susceptible to post-fire flooding due to its steep slopes, vegetation loss due to fire, and increased soil hydrophobicity. Alluvial C14 chronology from the Schultz Creek Watershed, an adjacent watershed, show that sediment has been accumulating in the ephemeral channel for approximately 7,000 years without major fires or flooding (Stempniewicz, 2014). Regional channel geometry observations support this chronology, with the majority of bankfull channel area in forested watersheds being undersized for the area of the watershed indicating complacent rainfall-runoff conditions (Schenk et al. 2021). A similar absence of recent fire and flooding is also expected for the SWW, leaving significant quantities of sediment available to mobilize during storms.

1.3 Northern Arizona's climate makes it susceptible to post-fire debris flows and flash flooding. The climate is characterized by four distinct seasons, a cold snow-dominated winter, a dry and windy late-spring/early summer, a wet late summer, and a temperate fall. Most of the region's precipitation occurs during the winter, in the form of snow, and in summer, when convective monsoonal storms occur (Jurwitz, 1953). Wildfire season typically extends from late May to early July, when conditions are commonly dry, hot, and windy. However, from July to September, precipitation from monsoonal storms raises the soil moisture and lowers the region's fire risk (Nauslar et al., 2019). These summer convective storms are characterized by high

intensity, short-duration rainfall events that are capable of producing flash-flooding even in unburned terrain (Adams & Comrie, 1997). When these storms occur over recently-burned, hydrophobic soils, the risk of post-fire runoff (i.e debris flows and flooding) is greatly increased (DeBano, 2000). Climate change projections for the southwestern United States predict drier conditions, reduced snowpack, higher temperatures, and increased extreme weather events (Barnett et al., 2005, 2008; Brown et al., 2004; Cook et al., 2004). These changing conditions will likely lead to increased wildfire frequency and severity across the region, as well as, extreme weather events which together increase the likelihood of catastrophic mass-wasting events.

The combination of the monsoon directly following wildfire season makes Arizona extremely susceptible to post-fire flooding (Staley et al., 2020). This risk is particularly acute when wildfires occur in regions of steep topography adjacent to population centers. For the Museum Fire, the high likelihood of flooding and debris flows from the burn area and the proximity to a population center led us to deploy a network of seismometers and other monitoring equipment to detect and characterize these events. The 2019 monsoon season was the driest on record at the time, until it was surpassed by the 2020 season. Because the 2019 and 2020 monsoon seasons were abnormally dry, only a few convective storms occurred which produced few debris flows and flood events. Damage from these events was limited to USDA Forest Service land. The 2021 monsoon season was substantially wetter than average and several major, high-intensity storms occurred during July and August (Table 1). These storms triggered multiple episodes of flooding and debris flows. The debris flows repeatedly caused significant damage to the main Forest Service road to the area, but were limited to Forest Service lands. However, flood flows continued downstream, impacting numerous properties and buildings within the City of Flagstaff including an elementary school.

1.3 Post-fire debris flow detection and monitoring present observational challenges. It is difficult to predict when and where convective precipitation will occur within a large burned area and where slopes will destabilize. Currently, most monitoring of post-fire debris flows is done using cameras, rain gauges, and stream gauges (e.g., Kean et al., 2001; McGuire and Youberg, 2020; Raymond et al., 2020).. Seismic monitoring is a promising tool that can supplement these observations and allow us to better understand debris flow and flood initiation conditions and track propagation through a watershed. Seismic observations are ideal for this purpose as the instruments are designed to work in a range of extreme weather conditions, are unaffected by light levels, record debris flow energy from 10s to 100s of meters away in most cases, and do not have to be located within or aimed at a specific hillslope or segment of channel. Further, these instruments are frequently telemetered from remote locations with a latency of <1 minute between data collection and public availability (Benson et al., 2012; Trabant et al., 2008). The rapid availability of data from seismic monitoring systems, which are often designed for near real-time earthquake detection, location, and early warning, make seismic instruments an ideal candidate for debris flow and flash flood detection and early warning.

1.4 The use of seismic monitoring for detecting and characterizing debris flows is part of a recent expansion in the use of seismic analyses for non-traditional applications. These applications include using seismic data to monitor surface processes including estimating bed load in rivers and characterizing mass wasting events (Bessason et al., 2017; A Burtin et al., 2008, 2009, 2014; Arnaud Burtin et al., 2011, 2013; Cornet et al., 2005; Coviello et al., 2019; Ekstrom & Stark, 2013; Kean et al., 2015; Lai et al., 2018; Marineau et al. 2019; Roth et al., 2014, 2016; Schmandt et al., 2013; Tsai et al., 2012; Walter et al., 2017). In this work we apply and build on previous theoretical and observational work applying seismic observations to better

understanding debris flow properties (Allstadt, 2013; Bessason et al., 2017; Coviello et al., 2019; Farin et al., 2019; Kean et al., 2015; Lai et al., 2018; Zhang et al., 2021).

The primary source of seismic energy during debris flows and floods is the collision of sediment particles with the channel bed (Kean et al., 2015; Lai et al., 2018; Tsai et al., 2012). Theoretical work shows that the amplitude and frequency content of a debris flow seismic signal is controlled by a combination of flow properties, the nature of the impacts, distance from the seismic instrument, channel properties, and subsurface properties. Debris flow properties include particle size and density, flow area (length and width), flow depth, velocity, and the ratio of solids to liquid within the flow (Farin et al., 2019; Lai et al., 2018; Roth et al., 2016; Tsai et al., 2012). Of these many factors, debris flow velocity, magnitude, particle size, distance from the station, and channel and subsurface properties have the greatest impact on the observed signal (Farin et al., 2019). In the following sections we discuss how we can constrain these factors to better understand post-fire debris flows, floods, and other seismic signals in post-fire environments.

2 Data and Methods

2.1 Seismic instruments were deployed to detect and characterize debris flows for three summers following the Museum Fire (2019, 2020, and 2021). Stations consisted of either L-22 short period instruments deployed using IRIS PASSCAL quick deployment boxes or Nanometrics Meridian Compact systems. In 2019, and 2020 15 and 12 instruments were deployed, respectively, in arrays designed to record events in as many drainages as possible. All seismic data are archived at the IRIS DMC and a summary of the data and its availability for the 2019 and 2020 deployments is described in (Porter et al., 2021). In 2021, efforts were scaled

back with only four Nanometrics instruments deployed for the monitoring efforts. These four stations were installed along the main drainages within the burn area. We deployed two in the upper watershed, and two in the lower watershed along the main stem of the SWW (Figures 1 and 2). We focus analyses on our observations of multiple debris flows in the upper watershed from the 2021 monsoon season.

In addition to seismometers, a network of cameras and rain gauges were also installed within the burn area for debris flow and flood detection and early warning (Figures 1 and 2). The camera network consisted of four telemetered cameras and six non-telemetered cameras. These cameras were aimed at the drainages where flooding was considered likely and are used to corroborate our seismic observations. Three rain gauges were installed within the burn area as part of a broader telemetered rain and stream gauge network operated by the City of Flagstaff. One existing rain and stream gauge within the burn area was upgraded after the fire. This publicly-available rain gauge network consists of 37 gauges designed to identify flood risks during monsoonal storms in the Flagstaff vicinity (Schenk et al. 2021).

2.2 We compare seismic data to rain gauge and radar observations oo better constrain debris flow initiation and behavior. We identify major rain events using data from four rain gauges located within the burn area. Based on observations from the 2019 and 2020 monsoon season, debris flows were deemed likely to occur during events that had 15-minute intensities greater than 30 mm or 60-minute intensities greater than 15 mm. Table 1 lists every storm that met at least one of those criteria at a minimum of one rain gauge within the burn area. Storm start times and durations are based on the timing that these thresholds are first and last exceeded by any gauge within the array. Table 1 highlights the localized nature of these convective monsoonal storms as extreme variations in rain intensity and storm total are observed over scales

of hundreds of meters to a few kilometers. For example, rain gauges Museum Fire North and Museum Fire East are located ~1 km apart and, in most storms, recorded significantly different peak intensities and total rainfall amounts.

Data from the National Weather Service Doppler-radar station (NEXRAD, WSR-88D) KFSX, located ~75 km SSE of Flagstaff, were integrated with gauge data to more accurately estimate the spatial extent and quantity of rainfall derived from radar data. To accomplish this, level-3 NEXRAD base reflectivity data collected at a 0.5-degree angle were downloaded and compared to rain intensities recorded at the rain gauges for each storm in 5 minute increments. A non-linear least squares fit was used to calculate the power law relationship between radar reflectivity (Z in $mm^6\ m^{-3}$) and rainfall intensity (R in mm hr^{-1}) by solving for a_r and b_r in the Z-R relationship equation (e.g., Marshall et al., 1947):

$$R = \left(\frac{1}{a_r}\right)^{(1/b_r)} Z^{(1/b_r)} \qquad (1)$$

for each storm. This was accomplished by calculating intensity at 5-minute increments at each rain gauge (R) and comparing these to radar power (Z) for the same time period and location. All variables are listed in the Supplementary Data. Using all Z and R data available, we determine a_r and b_r values for each storm using a non-linear least squares fit for Z values less that 60 db. In this fit, data were weighted by the inverse of the distance from the center of the Museum Fire burn area to ensure that rainfall estimates were most consistent with rain gauge data in the study area. Using the calculated a_r and b_r values for each storm, radar-derived intensities were summed to calculate rainfall totals. Rainfall amounts and intensities from radar were then compared to the timing of debris flow initiation determined from seismic data.

2.4 Seismic data were processed to assess the efficacy of purpose-built arrays for detection and characterizing post-fire debris flows. Data were archived at the IRIS DMC and then downloaded for debris flows that occurred during the 2021 monsoon season. Raw data were tapered, detrended, demeaned, filtered between 1 and 99 Hz, and the instrument correction was applied to transfer the signal to ground velocity using the IRIS DMC data services. The data were then downloaded and resampled to 200 Hz. To better quantify the seismic signal associated with debris flows, we calculated signal power and short-time Fourier transforms of the processed data to generate spectrograms of the signals. Using these short-time Fourier transforms we estimate the peak frequency (f_{max}) and spectral centroid (f_{cent}) over a moving window to assess how these observations and wave polarizations change based on the type of seismic source.

Wave polarization characteristics were calculated using the following equations (Jones et al., 2016; Jurkevics, 1988; Vidale, 1986):

$$P = 1 - \left(\frac{2\lambda_3}{\lambda_1 + \lambda_2}\right) \quad (2)$$

$$I = \left(\frac{\sqrt[2]{Re(v_{12}^2) - Re(v_{13}^2)}}{Re(v_{11})}\right) \quad (3)$$

$$\theta = \left(\frac{Re(v_{13})}{Re(v_{12})}\right)$$

Where P is planarity, I is incidence angle, (is the azimuth, and ⌊i and v_{ij} are the eigenvalues and eigenvectors for a time window, respectively. The variables i and j can equal 1, 2, or 3 and represent the different eigenvalues and the three components of the eigenvectors in the coordinate frame, respectively. Planarity values can range from 1 to 0, with 1 representing a wavefield polarized into a plane and 0 representing a wavefield with motion equally distributed in three directions. Incidence angle and azimuth range from -90° to 90° and 0° to 180°, respectively, and give insight into the orientation of the first eigenvector. This provides information into the orientation of ground motion, which is useful for discerning the source of the seismic signals.

2.5 We calculate synthetic models of the seismic signal power and spectral content associated with noise, rainfall, and debris flows in order to better interpret our results,. Though we do not attempt to match our observations exactly, these calculations are useful for providing context to our observations and for exploring the sensitivity of seismic data to variations in debris flow properties.

Approximations of background noise, much of which was likely due to wind interacting with trees, were calculated by using recordings of the seismic signal in the hours preceding storms. We transformed these data to the frequency domain where we applied a spline interpolation to calculate frequency envelopes of these data. We then selected random amplitudes in the frequency domain between the frequency envelope minimum and maximum values. These values were then inverse Fourier transformed back to the time domain. This resulted in a pseudo-random signal with a frequency content and amplitude similar to the

252 background noise observed at the seismic station. This signal was input as the background signal
253 in our synthetic models to represent noise.
254
255 2.6 To model rainfall, we follow a similar methodology to Bakker et al., (2022) where we
256 assume consistent rainfall in all directions from the seismic instrument. For reasonable rain drop
257 size of 0.1-8 mm, an impact should occur over less than 0.001 second and can be assumed as an
258 infinite frequency source for seismic purposes. We calculate the signal power density (*PSD*) as a
259 function of frequency (*f*) using the equation:
260
261 $$PSD(f) = (2\pi f)^2 \int_0^\infty 2\pi J_p G(f,r)^2 \, dr$$
262 *5*
263
264 Where *r* is the distance from the station, J_p is the impulse flux, and *G(f,r)* is the Green's
265 function.
266 We calculate impulse flux by summing the impact forces for a distribution of raindrop
267 sizes described by *p(d)* using the following equation:
268
269 $$J_p = \left(\frac{4}{3}\pi\rho_w\right)^2 \gamma \sum (0.5p(d))^6 v(p(d))^2$$
270 *6*
271

Where d is drop diameter, $\rangle_w$ is the density of water, © described the elasticity of the impact, and $v(p(d))$ is the velocity of drops as a function of diameter. We assume an inelastic impact with the ground which gives us a © value of 1. We estimated $p(d)$ to calculate the impact rate per unit area following (Uijlenhoet & Stricker, 1999) where raindrop size distribution is a function of rain intensity.

$$p(d) = \frac{\Lambda^{1+\beta}}{\Gamma(1+\beta)} d^{B} e^{-\Lambda d}$$

(7)

Where $\not<=4.1R^{-0.21}$, $\wp$ is the gamma function, and ® = 0.67 (Uijlenhoet & Stricker, 1999).

Drop velocity is calculated as $v(d) = ad^{B}$ (Atlas & Ulbrich, 1977) with constants a and B equal to 3.778 and 0.67, respectively (Uijlenhoet & Stricker, 1999). In this relationship, we set 9.5 m/s as a maximum raindrop velocity (Bakker et al., 2022). This assumption has little effect on the results, as even at high intensities where large drops are expected, few rain drops are large enough to exceed this velocity.

Surface waves are expected to dominate the observed environmental signals, so we use a near-field approximation of the Rayleigh wave Green's function (Aki & Richards, 2002; Bakker et al., 2022; Gimbert et al., 2014) which is calculated as follows:

$$G(f,r) = N_{jz}\frac{f}{8p_0 v_c^2 v_u}\left(1+\left(\frac{\pi^2 fr}{v_c}\right)^3\right)^{\frac{-1}{6}} e^{\frac{-\pi fr}{v_u Q}} \quad (8)$$

Where f is frequency, ρ_0 is the density at the surface, v_c is the phase velocity, v_u is the group velocity, r is the source-receiver distance, Q is the quality factor, and N_{jz} is a unitless value that described the relative amplitudes of the three components (the z subscript indicates the vertical component). At high frequencies, where rain is observed seismically, N_{jz} is near unity (Tsai & Atiganyanun, 2014) so we assumed a value of 1 for rain. Phase (v_c) and group velocities (v_u) are calculated for Rayleigh waves following (Tsai & Atiganyanun, 2014) where:

$$v_c(f) = v_{c0}\,(f/f_0)^{-\xi} \quad (9)$$

$$v_u(f) = v_c\,(f)^{(1+\xi)} \quad (10)$$

Where ξ describes the velocity change with depth, f_0 is a reference frequency set to 1 Hz and v_{c0} is a reference phase velocity.

2.7 Debris flow signal power was calculated using an equation to estimate seismic energy for a thin flow (Farin et al., 2019):

315 $$PSD(f\ ,r\ ,D) = \int (2\pi f)^2 {N_{jz}}^2 {I_j}^2 R_{impact} W G(f,r)^2\, dr$$

316 *11*

317

318 Where *f* is frequency, *r* is distance from the station to points along the channel, *W* is
319 channel width, and *G* is the Green's function defined above. R_{impact} is the impact rate calculated
320 as $R_{impact} = \frac{u_x \phi p(D)}{D_b D^2}$ where u_x is the velocity of the flow, ϕ is fraction of the flow volume that
321 consists of solids, *p(D)* is the grain size distribution, D_b is the bed bump-diameter, and *D* is grain
322 size. The impulse I_j is defined as $I_j = (1 + e_b) u_x m f_j$, where e_b is the basal coefficient of
323 restitution, *m* if the particle mass, an f_j is a unitless value related to speed change during particle
324 impact.

325

326 Assuming a linear channel oriented in the x direction located at a distance r_0 from the
327 station at its closest point and the same Green's function as above. This equation becomes:

328

329 $$PSD(f\ ,r_0\ ,x\ ,D) = R_{impact} W {N_{jz}}^2 {I_j}^2 \frac{\pi^4 f^4 (1+e_b)^2 m^2 {u_x}^2 r_0}{4 {p_0}^2 {v_c}^4 {v_u}^2} \int_{x_{min}/r_0}^{x_{max}/r_0} \left(1 + \left(\frac{\pi^2 f r_0 \sqrt{1+y^2}}{v_c}\right)^3\right)^{\frac{-1}{3}} e^{\frac{-2\pi f r_0 \sqrt{1+y^2}}{v_u Q}} dy$$

330 *12*

331 Where $y = \frac{x}{r_0}$ and x = 0 at the closest point in the channel to the station.

332

333 We follow previous work and use a log-raised cosine grain size distribution (Farin et al.,
334 2019; Tsai et al., 2012) with a standard deviation of 0.5 to calculate the grain size distribution
335 (*p(D)*) of the flow, which is input for *D* in Equation 11.

Rather than assume a constant mean grain size (D_{mean}) for the snout and body of the debris flow, we calculate mean grain size as a function of x by combining a decay function with a decaying sine function:

$$D_{mean} = 0.05 + 0.1\, e^{-0.01\left(\frac{x_{max}}{r_0} - y\right)} + 0.2\, e^{-0.1\left(\frac{x_{max}}{r_0} - y\right)} \left(\frac{2\pi r_0}{x} \left(\frac{x_{max}}{r_0} - y \right) \right)$$

This mean grain size equation was chosen to simulate short duration increased signal power due to pulses of coarse grain sediment moving down channel and the decay of the signal in the observed data.

3 Results and Discussion

3.1 Seismic records from our deployment affirm the efficacy of seismic monitoring in post-wildfire settings. These instruments can be installed rapidly following wildfires in locations that are safe from inundation (i.e. hillslopes or bedrock away from a channel). They produce clear recording of debris flows and related phenomena regardless of lighting or weather conditions. During monsoonal storms, we commonly observe signals associated with wind, lightning, storm precipitation, and storm-induced debris flows and flood flows. Each signal is associated with distinct signal powers, frequency content, and ground motion polarizations. We show ground velocity, signal power, and spectrograms for vertical component seismic data in both our synthetic and observed data, though the signals can also be observed in the horizontal components. In analyzing these seismic signals, we can differentiate between the different

358 sources, estimate the timing of lightning strikes, rainfall intensity, rainfall kinetic energy, and
359 debris flow timing, size, velocity, and location.

360 3.2 The seismic signal from wind is frequently site specific and can vary over short
361 spatial scales due to differences in aspect, vegetation, and infrastructure (Johnson et al., 2019).
362 To explore the site-specific wind signal, we use seismic recordings of windy days in the early
363 summer where no precipitation occurred. Figure 3 shows the seismic signal observed on June 27,
364 2021 when wind speeds recorded at the Flagstaff airport between 10:00 and 18:00 h, local time,
365 ranged between 10 and 13.2 m/s with a maximum gust of 23.2 m/s. (Visual Crossing, 2022). At
366 site E19A, located in the upper watershed, we observe wind as a low frequency signal ($f_{max} < 20$
367 Hz) on that day. The mean signal power during that recording period was ~142 dB, which is
368 substantially lower than signal powers associated with lighting, precipitation, and debris flows.
369 Energy polarization of wind recordings at E19A shows variable azimuthal directions, planarity
370 values of ~0.65, and incidence angles near horizontal.

371 3.3 Lightning is observed as impulsive, short duration (generally < 10 s) signals that
372 excite a wide range of frequencies (Figure 4). These are most easily observed prior to debris flow
373 and rainfall signals. We compare seismic recordings to records of lightning strikes from National
374 Lightning Detection Network (NLDN; Cummins & Murphy, 2009; Murphy et al., 2021; Orville,
375 2008). Seismic detection of lightning is likely impacted by topography and atmospheric
376 conditions. Lightning tends to have high incidence angles and variable planarity and azimuth
377 values associated with it (Figure 4). It is distinguishable from rain due by its short duration,
378 frequency content, and high amplitudes.

379 3.4 During storms, we commonly observe relatively high frequency (> 50 Hz) signals due
380 to precipitation (Figure 4). The amplitudes of these signals correlate temporally with estimates of

rainfall intensity observed at nearby rain gauges. However, given the highly localized nature of monsoonal storms in the southwestern US (Table 1), if the instruments are not co-located, there is often a lag between seismic and rain gauge observations associated with storms moving across the landscape. Theoretically the seismic signal of rain is controlled by the Green's function, rain drop quantity, and drop size distribution (which also controls the distribution of drop velocities; Bakker et al., 2022). Peaks in seismic signal power correlate well with increases in rainfall intensity (R) at nearby rain gauges. For station E19A, polarization analysis shows that rainfall has high incidence angles, moderate (~0.5) planarity, and variable azimuths, which is consistent with measurements of rainfall recorded at other stations. The high frequency content of the signal is due to the proximity of rainfall to the station. Work by Bakker et al. (2022), shows that, due to signal attenuation, over half of the energy observed at a station due to rainfall come from raindrops within 10 m of the station and 90% from drops within 25 m.

3.5. Debris flows are observed as high amplitude signals that may excite a range of frequencies (Figures 5 & 6). The signal power at a station increases rapidly as the debris flow approaches the station and then gradually decreases as the flow velocity and grain size decrease over time. Consistent with theoretical work, the frequency content of these flows appears to be controlled by the distance between the station and the debris flow and subsurface properties (i.e., the Green's function; Farin et al., 2019; Lai et al., 2018). We observe a decrease in seismic frequency (f_{max} and f_{cent}) as the snout of the flow first approaches the station followed by an increase, which is consistent with a signal frequency content dominated by attenuation (Farin et al., 2019; Lai et al., 2018; Tsai et al., 2012). The initial decrease in f_{max} and f_{cent} is due to the increased contribution of the debris flow to the seismic signal relative to rain, wind, and other background noise. Once the debris flow is the dominant signal, the increase in frequency content

404 is due to the debris flow snout approaching the station. Within individual debris flows, we
405 observe multiple changes in frequency content and signal power over short periods of time.
406 Values measured for f_{max} and f_{cent} often produce a sawtooth pattern. These changes in amplitude
407 and in frequency content are likely due to pulses of coarse-grained sediments moving through the
408 system and approaching the seismometer. The peaks in amplitude and f_{max} occur when coarse
409 sediment is in closest proximity to the station.

410 In Figures 5 and 6 we show records of two storms and associated debris flows recorded at
411 station E19A, located in the steeper upper watershed (Figure 1). This station was installed ~20 m
412 due north of a drainage that was deemed likely to experience debris flows. As an example of the
413 data recorded at this station, on July 16, 2021 we observed two separate debris flows in a short
414 period between 13:00 and 14:00 h local time. Prior to the flows, we observe several lightning
415 strikes (Figure 4) followed by a signal we associate with rainfall. Rainfall intensity at the
416 Museum Fire north gauge peaked at ~13:14, which coincides temporally with a peak in high
417 frequency seismic energy (> 50 Hz) at the station. At 13:16 a low frequency signal (< 20 Hz) is
418 first recorded that is likely caused by flow in the channel. There is also a higher frequency signal
419 (> 30 Hz) observed at this time from an ambiguous source. The energy that produced this signal
420 may have been caused by sediment transport in the channel, however we would not expect a
421 "gap" in energy at ~25 Hz or an f_{max} with a higher frequency than observed when the debris flow
422 snout is in closest proximity to the station if that were the case. Alternately, this signal was
423 possibly caused by sheet flow on the hillslope near the station, which would result in a higher
424 frequency signal due to the proximity of the station to the flow.

425 The low frequency signal, first observed at 13:16, begins increasing in amplitude and
426 frequency at ~13:17 (Figure 4). This is likely due to the snout of the debris flow approaching the

station. This signal peaks in amplitude just after 13:18, which is when the snout reaches its closest point in the channel to the station. Following the initial debris flow snout signal, we observe multiple high amplitude pulses between 13:18 and 13:24. These signals produce a sawtooth pattern in observed f_{max} and f_{cent} values. These power and frequency patterns are likely due to multiple pulses of coarse sediment, separated by finer grained flow, traveling down the channel. After the initial high amplitude signal, the overall amplitude of the debris flow signal power decreases, which is likely due to decreases in discharge, velocity, and grain size. The debris flow produces the largest signal power at the station until ~13:27 when an increase in rainfall intensity occurs. This change in signal source is inferred based on a change in frequency content and energy polarization that occurred at that time. Rainfall is the highest amplitude signal until ~13:29 when a second debris flow is observed in the seismic data. The signal from this second flow is similar to the first. It exhibits increased signal power initially followed by multiple pulses of increased amplitudes and sawtooth changes in f_{max} and f_{cent}. After peaking, this signal gradually decays back to baseline (pre-storm) values.

On August 17, 2021, we observe a similar signal to the July 16th events (Figure 6) at station E19A, demonstrating the consistency of debris flow signal at the station. For this August debris flow, a remote game camera installed ~90 meters upstream recorded sediment transport (Figures 6b and 6c). Photos were taken at 5 minutes intervals with an uncertainty of ~1 minute on the timestamp. These images capture high intensity rainfall and sheet flow prior to the debris flow which is observed in the second image. Due to the uncertainty on the game photo timings and the difference in locations, we cannot precisely tie the photos directly to seismic observations. However, based on these timings, it seems probable we are observing sheet flow or

similar in the initial higher frequency energy followed by sediment pulses (including downed trees) during the main flow.

Based on an analysis of multiple events recorded at station E19A, debris flows at this station are characterized by a low incidence angle, a high planarity, and an azimuth measurement oriented roughly NS. This NS azimuth is the direction from the station to the nearest point in the channel. Polarization measurements at this station are more-consistent than those observed at other stations, but in general, we observe consistent azimuths, moderate planarities and low incidence angles in debris flow signals regardless of the station.

3.6 Using the equations in section 2, we generate synthetic models of signal power and spectral content for sources that include background noise, rainfall, and debris flow signals. For the Green's function, inputs were selected to match the frequency content of rain and the debris flows recorded at station E19A on July 16th (Figure 5). In our synthetic models (Figure 7) we reproduce the initial high frequency signal associated with rain using a rainfall intensity of 100 mm/hr for the first 450 seconds of the signal. As the modeled debris flow approaches the station, we observe a decrease in f_{max} and f_{cent} which occurs when the debris flow becomes the dominant signal. The subsequent increase in f_{max} and f_{cent} and the sawtooth patterns observed in the data are modeled using a sine function (Equation 13) to represent pulses of increased sediment size moving down the channel. As this sine function decays, the f_{max} value becomes more stable and is consistent with the strongest seismic signal originating from the closest point in the channel to the seismometer. Finally, the decay in signal amplitude is produced by decreasing the mean grain size. In reality, this is a simplification of the process as the decay in amplitude observed in our recorded data is likely due to decreases in mean grain size, flow velocity, and flow volume.

Results from this work confirm the validity of theoretical models for understanding post-wildfire debris flow behavior. Observed and model results are consistent with signal power correlating with the velocity and the grain size of a flow (D_{mean}). The highest amplitude observed in most flows corresponds to the snout passing by the station. Additional high-amplitude peaks likely are indicative of sediment pulses within the flow passing by the station. The peak in signal power within these pulses occurs when the coarse sediment is in closest proximity to the station. The frequency content of debris flow is primarily controlled by the distance of the flow from the station. However, this frequency content can also provide insight into the behavior of a flow. The sawtooth pattern in frequency content (f_{max} and f_{cent}) observed during debris flow events is likely due to coarse sediment pulses moving down the channel. Pulses with large grain sizes produce higher amplitude seismic signals, so even when they are farther from the station than smaller-grain sized flows, they still may produce a large enough signal to lower the f_{max} and f_{cent} measurements. For a long flow with consistent grain size distribution and velocity, we would expect a signal with consistent frequency content. This is often observed later in flows when the f_{max} measurements become fairly consistent, likely indicating that the debris flow is no longer moving downslope in pulses or has evolved into a finer-grained flow. The f_{cent} measurement continues to change later in flows as the grain size decreases and there are less contributions from sediment transport further away in the channel to the recorded signal.

3.7 Debris flow velocity can be estimated by examining the frequency content of the seismic signal or the cross-correlation of signals between stations based on equation 11. At station E19A, we estimate velocities of the debris flow's snout following Lai et al. (2018) who show that debris flow frequency content is controlled by the Green's function and source-flow distance. To accomplish this, we calculate $dP/df = 0$ for Equation 11 and solve for r using f_{max} as

494 the input frequency. We then use the Pythagorean theorem to calculate the along-channel x
495 location of the front of the flow, with *r* as the hypotenuse and r_0 and x as the legs. In this
496 calculation, x = 0 at the point in the channel closest to the station. To calculate smoothed f_{max}
497 values from our data, we use least squares fit to the observed f_{max} values as the flow approaches
498 the station. The linear fit is used for simplicity in both estimating f_{max} and velocity. Using this
499 approach, we estimate a velocity of ~6 m/s for the first debris flow that occurred on July 16th
500 (Figure 8). While we apply this technique to calculate the velocity of the initial debris flow
501 snout, this also can be applied to calculate the velocity of individual sediment pulses which can
502 be used to estimate changes in flow velocity over time.

503 The four stations used during the 2021 deployment did not allow us to measure debris
504 flow velocities using cross correlation as we did not have multiple stations within any drainage
505 in the upper watershed. However, we show an example from lower in the watershed downstream
506 of where a majority of the coarse material was deposited (Figure 9). We normalize and then
507 cross correlate the signal between stations COCB and CFSG, which were located ~1.2 km from
508 each other along the channel (Figure 9). The lag time of the cross correlations for an event on
509 July 13, 2021 was 360 seconds yielding an estimated velocity of 3.3 m/s for the flood in that
510 reach of the channel. Applying this to multiple events over the summer led to velocity estimates
511 between 2.6 m/s and 4.1 m/s for the reach.

512 3.8 Constraining the Green's function at a station can present a challenge, especially in
513 post-wildfire settings where stations are frequently deployed on steep unstable slopes and access
514 may be limited due to hazards to personnel. However, if the rainfall rate is well-constrained by
515 rain gauge data and the drop size distribution can be estimated, the frequency content and power
516 of the rainfall seismic signal could provide a mechanism for calculating local high-frequency

Green's functions. Future work will explore methodologies for better calculating these Green's functions using rainfall data. Given that debris flows can alter the subsurface through scouring and deposition, an analysis of the rainfall may provide a mechanism for assessing these changes. Additionally, examining the frequency content of a debris flow signal can provide insight into the Green's function. The highest frequency f_{max} value associated with the debris flow will be observed when the debris flow is at the point in the channel that is in closest proximity to the station. If the distance between the station and the channel is known, this value can then be used as a constraint on the Green's function values. Though we do not attempt to replicate this exactly, the input values for our forward model were selected to roughly match the signals produced by rainfall and debris flow at station E19A.

3.9 Initial results indicate that wave polarization may be a good differentiator between seismic sources in post-fire settings. At station E19A, the signal azimuth, calculated using equation 4, is oriented towards the closest point in the channel to the station during debris flows. The signal associated with debris flows exhibits a higher planarity than other environmental events (i.e. wind, rain, lightning, etc.). The incidence angle is high during rain and low during debris flows, which may be related to the frequency content of the two signals. Work by (Tsai & Atiganyanun, 2014) shows that N_{jz} approaches unity at high frequencies while the amplitudes of horizontal components are diminished. Lower frequency surface waves have more energy on the horizontal components and less on the vertical. This is consistent with what we observe with rain ($f > 50$ Hz) and debris flows ($f > 5$ Hz).

3.10 Comparison to earthquakes and other energy sources affirms that debris flows produce a signal that is easily distinguishable from other sources of seismic energy even in sites hastily installed in suboptimal condition (steep slopes, shallow burial etc.). Over the course of

our monitoring, debris flows produce the highest amplitude signal observed in the 1-50 Hz frequency range. Additionally, the signal is much more emergent and longer duration than a typical earthquake signal. Simply measuring the short-term average to long-term energy averages works well for detecting events with the thresholds set depending on the size of the drainage and the flood/debris flow risk to downstream communities. If installed and telemetered, these instruments would complement existing monitoring which is frequently done with rain and stream gauges, cameras, and non-vented pressure transducers that, incidentally, are often lost or destroyed when a debris flow passes.

4 Conclusions

In this study we show data and interpretations for storms and debris flows recorded by seismic equipment in a post-fire setting. Results from this work affirm the validity of theoretical models of debris flow seismic energy generation and their applicability to quantifying debris flow characteristics in post-fire environments. Further, this work demonstrates the applicability of seismic monitoring for debris flow detection in this setting. Using seismic data, we are able to detect and distinguish seismic energy due to wind, lightning, rainfall, and debris flows/floods, demonstrating the efficacy of seismic data for event characterization and flood detection and early warning in these settings. Future work will build on this effort and better constrain and characterize post-wildfire debris flow behavior using seismic data.

Acknowledgments, Samples, and Data

The datasets generated for this study can be found in the following online repositories: https://doi.org/10. 7914/SN/1A_2019, https://www.flagstaff.az.gov/4111/Rainfalland-Stream-

Gauge-Data. Data availability and access is described in detail in a data report on the project available here: https://doi.org/10.3389/feart.2021.649938.

The funding for this project was provided by a National Science Foundation Grant: RAPID: Seismic Monitoring of Post-Fire Debris Flows Associated with the Museum Fire, Northern Arizona EAR 1946321, the US Department of Agriculture, Forest Service, Coconino National Forest (20-CS-11030400-101), the City of Flagstaff, AZ and Coconino County, AZ. The seismic instruments were provided by the Incorporated Research Institutions for Seismology (IRIS) through the PASSCAL Instrument Center at New Mexico Tech and by Northern Arizona University. Seismic data are available through the IRIS Data Management Center. The facilities of the IRIS Consortium are supported by the National Science Foundation's Seismological Facilities for the Advancement of Geoscience (SAGE) Award under Cooperative Support Agreement EAR-1851048.

Author JL is employed by the company JE Fuller Hydrology and Geomorphology, Inc.

Figure 1. Location map of the study area showing the burn area (shaded gray), seismic station locations, rain gauges, camera locations, drainages, and watershed boundaries. Colors indicate slopes.

Figure 2. Burn severity map for the Museum Fire (Museum Fire BAER Team, 2019; Figure 1). Shaded area denotes areas with moderate to high severity burn designations and slopes greater than 22° where debris flows are most likely.

Figure 3. Seismic recording of wind at station E19A. Panel a) shows ground velocity, storm rainfall total and 15-minute rainfall intensity (no rain accord during this time period). Panel b) shows decibel signal power. Panel c) is a spectrogram of the seismic velocity, black diamonds indicate the frequency with the maximum energy (f_{max}). Panel d) shows the spectral centroid (f_{cent}), color indicates the total signal power. Panel e) show the planarity, the absolute value of the cosine of incidence angle (0 is horizontal and 1 is vertical), and the normalized azimuth of the signal between 0 to 180°m where 0 is equal to 0° (due North) and 1 is equal to 180° (due south).

Figure 4. Seismic recording of lightning at station E19A. Panels are the same as Figure 3, except the amplitude scale in panel a) vertical black lines in panels b) and the timing of lightning strikes from the National Lightning Detection Network (NLDN) occurring within 12 km of the station

595 in panel c). Timings are adjusted from the NLDN timing to the estimated arrival time of thunder
596 at the station using a velocity of 330 m/s.

597 **Figure 5.** Seismic recording of debris flows at station E19A on July 16, 2021. Panels are the
598 same as Figure 3, except for amplitude scale in panel a).

599 **Figure 6.** Seismic recording of debris flow at station E19A on August 21, 2021. Top panels are
600 the same as Figure 3, except panel a) amplitude scale. Panels f) and g) show game camera
601 images of the channel before and during a debris flow. Images were taken at 12:14 and 12:19
602 local time, respectively.

603 **Figure 7.** Spectrogram for synthetic debris flow model. Blue circle are spectral centroid (f_{cent}),
604 black diamonds and the frequency with the maximum energy (f_{max}).

605 **Figure 8.** Panel a) changes in f_{max} over time beginning at 13:17:48 on July 16, 2022 at station
606 E19A. Red line is least-squares fit to the data. Panel b) along channel distance of the debris flow
607 snout calculated from f_{max} least squares fit in panel a). Red line is fit to the data, slope of the red
608 line is the velocity of the debris flow snout ~5.96 m/s.

609 **Figure 9**. Normalized signal power recorded at stations COCB and CFSG for an event on July
610 13, 2021. Cross correlating the signals results in a lag of 360 seconds between the two stations.

611 **Table 1.** Timing, Estimated Flow, Total Rain, Peak Intensity, Storm Direction and location, Peak
612 Flow at lower drainage for storms from 2019 to 2021.

613 **Supplementary Table 1.** List of symbols used in equations.

614

References

Abatzoglou, J. T., & Williams, A. P. (2016). Impact of anthropogenic climate change on wildfire across western US forests. *Proceedings of the National Academy of Sciences*, *113*(42), 11770–11775. https://doi.org/10.1073/pnas.1607171113

Adams, D. K., & Comrie, A. C. (1997). The North American Monsoon. *Bulletin of the American Meteorological Society*, *78*(10), 2197–2213. https://doi.org/10.1175/1520-0477(1997)078<2197:tnam>2.0.co;2

Aki, K., & Richards, P. G. (2002). *Quantitative seismology Second Edition*. University Science Books.

Allstadt, K. (2013). Extracting source characteristics and dynamics of the August 2010 Mount Meager landslide from broadband seismograms. *Journal of Geophysical Research: Earth Surface*, *118*(3), 1472–1490. https://doi.org/10.1002/jgrf.20110

Atlas, D., & Ulbrich, C. W. (1977). Path- and Area-Integrated Rainfall Measurement by Microwave Attenuation in the 1–3 cm Band. *Journal of Applied Meteorology*, *16*(12), 1322–1331. https://doi.org/10.1175/1520-0450(1977)016<1322:paairm>2.0.co;2

Bakker, M., Legout, C., Gimbert, F., Nord, G., Boudevillain, B., & Freche, G. (2022). Seismic modelling and observations of rainfall. *Journal of Hydrology*, *610*, 127812. https://doi.org/10.1016/j.jhydrol.2022.127812

Barnett, T. P., Adam, J. C., & Lettenmaier, D. P. (2005). Potential impacts of a warming climate on water availability in snow-dominated regions. *Nature*, *438*(7066), 303–309. https://doi.org/10.1038/nature04141

Barnett, T. P., Pierce, D. W., Hidalgo, H. G., Bonfils, C., Santer, B. D., Das, T., et al. (2008). Human-Induced Changes in the Hydrology of the Western United States. *Science*, *319*(5866), 1080–1083. https://doi.org/10.1126/science.1152538

Benson, R., Ahern, T., Trabant, C., Weertman, B., Casey, R., Stromme, S., & Karstens, R. (2012). Real Time Data for Seismology at the IRIS Data Management Center, AN Nsf-Sponsored Facility. In *AGU Fall Meeting Abstracts* (Vol. 2012, pp. IN33C-1555).

Bessason, B., Eiríksson, G., Thorarinsson, Ó., Thórarinsson, A., & Einarsson, S. (2017). Automatic detection of avalanches and debris flows by seismic methods. *Journal of Glaciology*, *53*(182), 461–472. https://doi.org/10.3189/002214307783258468

Brown, T. J., Hall, B. L., & Westerling, A. L. (2004). The Impact of Twenty-First Century Climate Change on Wildland Fire Danger in the Western United States: An Applications Perspective. *Climatic Change*, *62*(1–3), 365–388. https://doi.org/10.1023/b:clim.0000013680.07783.de

Burtin, A, Bollinger, L., Vergne, J., Cattin, R., & Nábělek, J. L. (2008). Spectral analysis of seismic noise induced by rivers: A new tool to monitor spatiotemporal changes in stream hydrodynamics. *Journal of Geophysical Research-Solid Earth and Planets*, *113*(B5), 911–14. https://doi.org/10.1029/2007jb005034

Burtin, A, Bollinger, L., Cattin, R., Vergne, J., & Nábělek, J. L. (2009). Spatiotemporal sequence of Himalayan debris flow from analysis of high-frequency seismic noise. *Journal of Geophysical Research-Solid Earth and Planets*, *114*(F4), 410–16. https://doi.org/10.1029/2008jf001198

Burtin, A, Hovius, N., McArdell, B. W., Turowski, J. M., & Vergne, J. (2014). Seismic constraints on dynamic links between geomorphic processes and routing of sediment in a

661 steep mountain catchment. *Earth Surface Dynamics*, *2*(1), 21–33.
662 https://doi.org/10.5194/esurf-2-21-2014
663 Burtin, Arnaud, Cattin, R., Bollinger, L., Vergne, J., Steer, P., Robert, A., et al. (2011). Towards
664 the hydrologic and bed load monitoring from high-frequency seismic noise in a braided river:
665 The â€œtorrent de St Pierreâ€•, French Alps. *Journal of Hydrology*, *408*(1–2), 43–53.
666 https://doi.org/10.1016/j.jhydrol.2011.07.014
667 Burtin, Arnaud, Hovius, N., Milodowski, D. T., Chen, Y.-G., Wu, Y.-M., Lin, C.-W., et al.
668 (2013). Continuous catchment-scale monitoring of geomorphic processes with a 2-D
669 seismological array. *Journal of Geophysical Research: Earth Surface*, *118*(3), 1956–1974.
670 https://doi.org/10.1002/jgrf.20137
671 Cook, E. R., Woodhouse, C. A., Eakin, C. M., Meko, D. M., & Stahle, D. W. (2004). Long-term
672 aridity changes in the western United States. *Science*, *306*(5698), 1015–1018.
673 https://doi.org/10.1126/science.1101982
674 Cornet, E. S., Guillén, I. V., Khazaradze, G., Górriz, B. B., Bellavista, G. F. i, & Vilaplana, J. M.
675 (2005). Seismic detection and characterization of landslides and other mass movements.
676 *Natural Hazards and Earth System Sciences*, *5*(6), 791–798. https://doi.org/10.5194/nhess-5-
677 791-2005
678 Coviello, V., Arattano, M., Comiti, F., Macconi, P., & Marchi, L. (2019). Seismic
679 Characterization of Debris Flows: Insights in to Energy Radiation and Implications for
680 Warning. *Journal of Geophysical Research: Earth Surface*, *12*(4), 4870–24.
681 https://doi.org/10.1029/2018jf004683
682 Cummins, K. L., & Murphy, M. J. (2009). An Overview of Lightning Locating Systems:
683 History, Techniques, and Data Uses, with an In-Depth Look at the U.S. NLDN. *IEEE*
684 *Transactions on Electromagnetic Compatibility*, *51*(3), 499–518.
685 https://doi.org/10.1109/temc.2009.2023450
686 DeBano, L. F. (2000). The role of fire and soil heating on water repellency in wildland
687 environments: a review. *Journal of Hydrology*, *231*, 195–206. https://doi.org/10.1016/s0022-
688 1694(00)00194-3
689 Ekstrom, G., & Stark, C. P. (2013). Simple Scaling of Catastrophic Landslide Dynamics.
690 *Science*, *339*(6126), 1416–1419. https://doi.org/10.1126/science.1232887
691 Farin, M., Tsai, V. C., Lamb, M. P., & Allstadt, K. E. (2019). A physical model of the high-
692 frequency seismic signal generated by debris flows. *Earth Surface Processes and Landforms*,
693 *44*(13), 2529–2543. https://doi.org/10.1002/esp.4677
694 Gimbert, F., Tsai, V. C., & Lamb, M. P. (2014). A physical model for seismic noise generation
695 by turbulent flow in rivers. *Journal of Geophysical Research: Earth Surface*, *119*(10), 2209–
696 2238. https://doi.org/10.1002/2014jf003201
697 Holm, R. F. (1988, January 1). Geologic map of San Francisco Mountain, Elden Mountain, and
698 Dry Lake Hills, Coconino County, Arizona. United State Geological Survey. Retrieved from
699 https://pubs.er.usgs.gov/publication/i1663
700 Johnson, C. W., Meng, H., Vernon, F., & Ben-Zion, Y. (2019). Characteristics of Ground
701 Motion Generated by Wind Interaction With Trees, Structures, and Other Surface Obstacles.
702 *Journal of Geophysical Research: Solid Earth*, *124*(8), 8519–8539.
703 https://doi.org/10.1029/2018jb017151
704 Jolly, W. M., Cochrane, M. A., Freeborn, P. H., Holden, Z. A., Brown, T. J., Williamson, G. J.,
705 & Bowman, D. M. J. S. (2015). Climate-induced variations in global wildfire danger from
706 1979 to 2013. *Nature Communications*, *6*(1), 7537. https://doi.org/10.1038/ncomms8537

Jones, J. P., Eaton, D. W., & Caffagni, E. (2016). Quantifying the similarity of seismic polarizations. *Geophysical Journal International*, *204*(2), 968–984. https://doi.org/10.1093/gji/ggv490

Jurkevics, A. (1988). POLARIZATION ANALYSIS OF THREE-COMPONENT ARRAY DATA. *Bulletin of the Seismological Society of America, 78*(5), 1725–1743.

Jurwitz, L. R. (1953). Arizona's two-season rainfall pattern. *Weatherwise*, *6*(4), 96–99.

Kean, J. W., Coe, J. A., Coviello, V., Smith, J. B., McCoy, S. W., & Arattano, M. (2015). Estimating rates of debris flow entrainment from ground vibrations. *Geophysical Research Letters*, *42*(15), 6365–6372. https://doi.org/10.1002/2015gl064811

Kean, J. W., and D. M. Staley (2011), Direct measurement of the hydrologic conditions leading up to and during post-fire debris flow in southern California, USA, in *Debris-Flow Hazards Mitigation, Mechanics, Prediction, and Assessment*, edited by R. Genevois, D. L. Hamilton and A. Prestininzi, pp. 685-694, Casa Editrice Univ. La Sapienza, Rome.

Lai, V. H., Tsai, V. C., Lamb, M. P., Ulizio, T. P., & Beer, A. R. (2018). The Seismic Signature of Debris Flows: Flow Mechanics and Early Warning at Montecito, California. *Geophysical Research Letters*, *45*(11), 5528–5535. https://doi.org/10.1029/2018gl077683

McGuire, L. A., and A. M. Youberg (2020), What drives spatial variability in rainfall intensity-duration thresholds for post-wildfire debris flows? Insights from the 2018 Buzzard Fire, NM, USA, *Landslides*, doi:10.1007/s10346-020-01470-y.

Marineau, M.D., Wright, S.A., Gaeuman, D., Curran, C.A., Stark, K., Siemion, J., and Schenk, E.R., 2019, Overview of five recent acoustic bedload monitoring field experiments using hydrophones, in Sediment surrogate measurements, sediment yield and fingerprinting, stream restoration, water quality, watershed management, v. 4 of Proceedings of SEDHYD 2019—Conferences on sedimentation and hydrologic modeling—Improving resiliency and sustainability of watershed resources and infrastructure, 1st, [4th Joint Federal Interagency Conference on Sedimentation and Hydrologic Modeling, a joint meeting of the 6th Federal Interagency Hydrologic Modeling Conference and the 11th Federal Interagency Sedimentation Conference], Reno, Nev., June 24–28, 2019: SEDHYD, Inc., 14 p.

Marshall, J. S., Langille, R. C. & Palmer. (1947). W. M. K. MEASUREMENT OF RAINFALL BY RADAR. *J Meteorol* **4**, 186–192.

Murphy, M. J., Cramer, J. A., & Said, R. K. (2021). Recent History of Upgrades to the U.S. National Lightning Detection Network. *Journal of Atmospheric and Oceanic Technology*, *38*(3), 573–585. https://doi.org/10.1175/jtech-d-19-0215.1

Nauslar, N. J., Hatchett, B. J., Brown, T. J., Kaplan, M. L., & Mejia, J. F. (2019). Impact of the North American monsoon on wildfire activity in the southwest United States. *International Journal of Climatology*, *39*(3), 1539–1554. https://doi.org/10.1002/joc.5899

Orville, R. E. (2008). Development of the National Lightning Detection Network. *Bulletin of the American Meteorological Society*, *89*(2), 180–190. https://doi.org/10.1175/bams-89-2-180

Parks, S. A., Miller, C., Parisien, M.-A., Holsinger, L. M., Dobrowski, S. Z., & Abatzoglou, J. (2015). Wildland fire deficit and surplus in the western United States, 1984–2012. *Ecosphere*, *6*(12), art275-13. https://doi.org/10.1890/es15-00294.1

Porter, R., Joyal, T., Beers, R., Loverich, J., LaPlante, A., Spruell, J., et al. (2021). Seismic Monitoring of Post-wildfire Debris Flows Following the 2019 Museum Fire, Arizona. *Frontiers in Earth Science*, *9*, 649938. https://doi.org/10.3389/feart.2021.649938

Radeloff, V. C., Helmers, D. P., Kramer, H. A., Mockrin, M. H., Alexandre, P. M., Bar-Massada, A., et al. (2018). Rapid growth of the US wildland-urban interface raises wildfire risk.

Proceedings of the National Academy of Sciences, *115*(13), 201718850. https://doi.org/10.1073/pnas.1718850115

Raymond, C. A., L. A. McGuire, A. M. Youberg, D. M. Staley, and J. W. Kean (2020), Thresholds for post-wildfire debris flows: Insights from the Pinal Fire, Arizona, USA, *Earth Surface Processes and Landforms*, *45*(6), 1349-1360, doi:10.1002/esp.4805.

Roth, D. L., Finnegan, N. J., Brodsky, E. E., Cook, K. L., Stark, C. P., & Wang, H. W. (2014). Migration of a coarse fluvial sediment pulse detected by hysteresis in bedload generated seismic waves. *Earth and Planetary Science Letters*, *404*(C), 144–153. https://doi.org/10.1016/j.epsl.2014.07.019

Roth, D. L., Brodsky, E. E., Finnega, N., Rickenmann, D., Turowski, J., & Badoux, A. (2016). Bed load sediment transport inferred from seismic signals near a river. *Journal of Geophysical Research: Solid …*, *121*(121), 725–747. https://doi.org/10.1002/2015jf003782

Sankey, J. B., Kreitler, J., Hawbaker, T. J., McVay, J. L., Miller, M. E., Mueller, E. R., et al. (2017). Climate, wildfire, and erosion ensemble foretells more sediment in western USA watersheds. *Geophysical Research Letters*, *44*(17), 8884–8892. https://doi.org/10.1002/2017gl073979

Schenk, E.R., Schiefer, E., Young, E., and C. Helton. 2021. Surface Water Hydrology and Flood Recurrence in the Flagstaff, Arizona Area, 2008-2019. City of Flagstaff Technical Report. Flagstaff, AZ 91 p. DOI: 10.4211/hs.8da8bb7cb66d475ea03af1a79b38a446

Schmandt, B., Aster, R. C., Scherler, D., Tsai, V. C., & Karlstrom, K. (2013). Multiple fluvial processes detected by riverside seismic and infrasound monitoring of a controlled flood in the Grand Canyon. *Geophysical Research Letters*, *40*(18), 4858–4863. https://doi.org/10.1002/grl.50953

Staley, D. M., Kean, J. W., & Rengers, F. K. (2020). The recurrence interval of post-fire debris-flow generating rainfall in the southwestern United States. *Geomorphology*, *370*, 107392. https://doi.org/10.1016/j.geomorph.2020.107392

Steel, Z. L., Safford, H. D., & Viers, J. H. (2015). The fire frequency-severity relationship and the legacy of fire suppression in California forests. *Ecosphere*, *6*(1), 1–23. https://doi.org/10.1890/es14-00224.1

Stempniewicz, V. A. (2014, December). *Evaluating erosion risk mitigation due to forest restoration treatments using alluvial chronology and hydraulic modeling*. Northern Arizona University.

Team, M. F. B. (2019). *Museum Fire Burned Area Emergency Response (BAER) Executive Summary*.

Trabant, C., Stromme, S., & Weertman, B. (2008). Managing a Torrent of Diverse Low-Latency Data Streams at the IRIS DMC. In *AGU Fall Meeting Abstracts* (Vol. 2008, pp. G43A-0666).

Tsai, V. C., & Atiganyanun, S. (2014). Green's Functions for Surface Waves in a Generic Velocity StructureShort Note. *Bulletin of the Seismological Society of America*, *104*(5), 2573–2578. https://doi.org/10.1785/0120140121

Tsai, V. C., Minchew, B., Lamb, M. P., & Ampuero, J.-P. (2012). A physical model for seismic noise generation from sediment transport in rivers. *Geophysical Research Letters*, *39*(2), L02404. https://doi.org/10.1029/2011gl050255

Uijlenhoet, R., & Stricker, J. N. M. (1999). A consistent rainfall parameterization based on the exponential raindrop size distribution. *Journal of Hydrology*, *218*(3–4), 101–127. https://doi.org/10.1016/s0022-1694(99)00032-3

Vidale, J. E. (1986). COMPLEX POLARIZATION ANALYSIS OF PARTICLE MOTION. *Bulletin of the Seismological Society of America*, *76*(5), 1393–1405.

Walter, F., Burtin, A., McArdell, B. W., Hovius, N., Weder, B., & Turowski, J. M. (2017). Testing seismic amplitude source location for fast debris-flow detection at Illgraben, Switzerland. *Natural Hazards and Earth System Sciences*, *17*(6), 939–955. https://doi.org/10.5194/nhess-17-939-2017

Westerling, A. L. (2016). Increasing western US forest wildfire activity: sensitivity to changes in the timing of spring. *Philosophical Transactions of the Royal Society B: Biological Sciences*, *371*(1696), 20150178. https://doi.org/10.1098/rstb.2015.0178

Westerling, A. L., Hidalgo, H. G., Cayan, D. R., & Swetnam, T. W. (2006). Warming and Earlier Spring Increase Western U.S. Forest Wildfire Activity. *Science*, *313*(5789), 940–943. https://doi.org/10.1126/science.1128834

Zhang, Z., Walter, F., McArdell, B. W., Haas, T., Wenner, M., Chmiel, M., & He, S. (2021). Analyzing Bulk Flow Characteristics of Debris Flows Using Their High Frequency Seismic Signature. *Journal of Geophysical Research: Solid Earth*, *126*(12). https://doi.org/10.1029/2021jb022755

Figure 1.

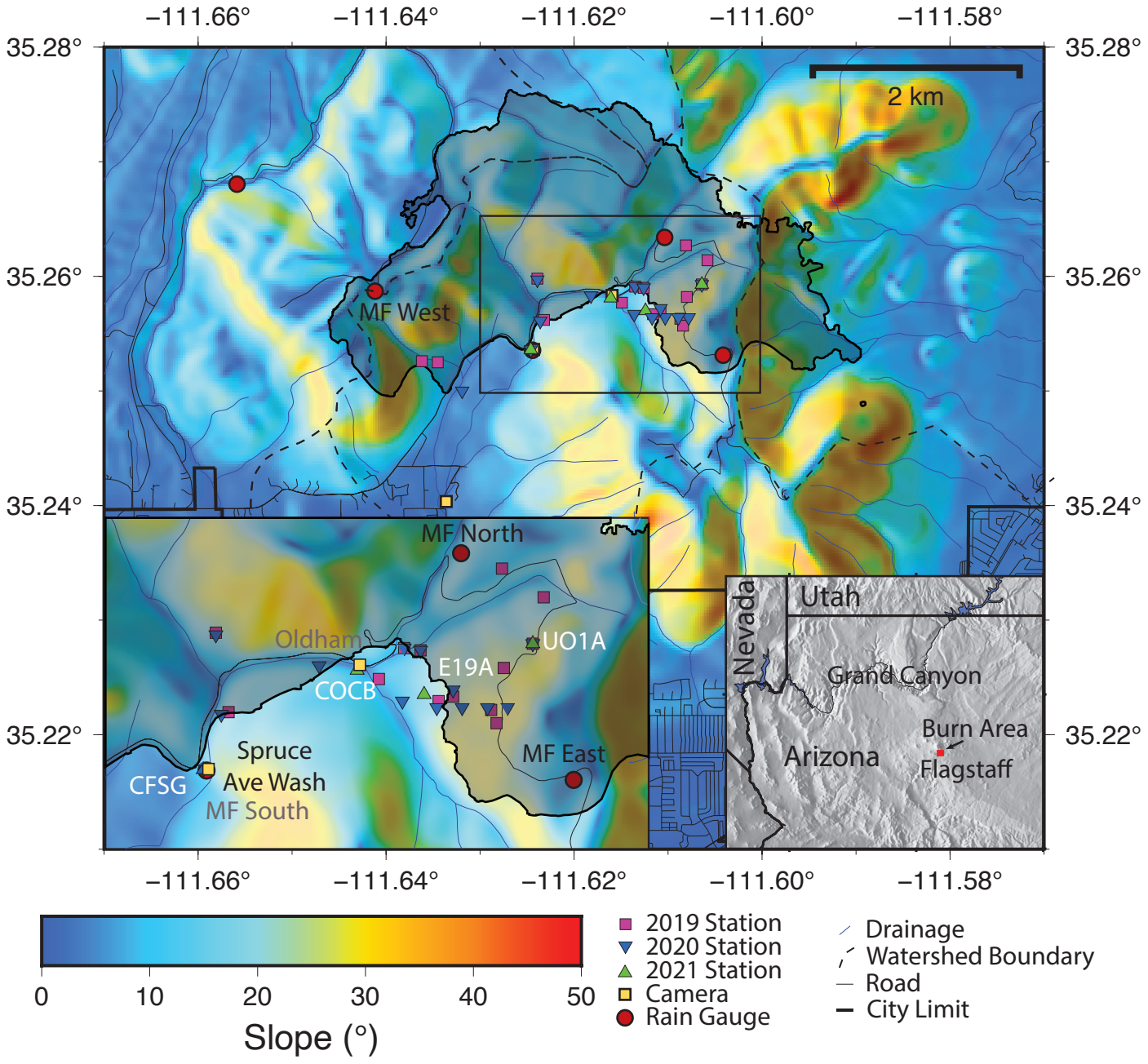
−111.66°
−111.64°
−111.62°
−111.60°
−111.58°
35.28°
35.26°
35.24°
35.22°
2 km
MF West
MF North
Oldham
UO1A
E19A
COCB
Spruce
Ave Wash
CFSG
MF South
MF East
Nevada
Utah
Grand Canyon
Arizona
Burn Area
Flagstaff
0
10
20
30
40
50
Slope (°)
2019 Station
2020 Station
2021 Station
Camera
Rain Gauge
Drainage
Watershed Boundary
Road
City Limit

Figure 2.

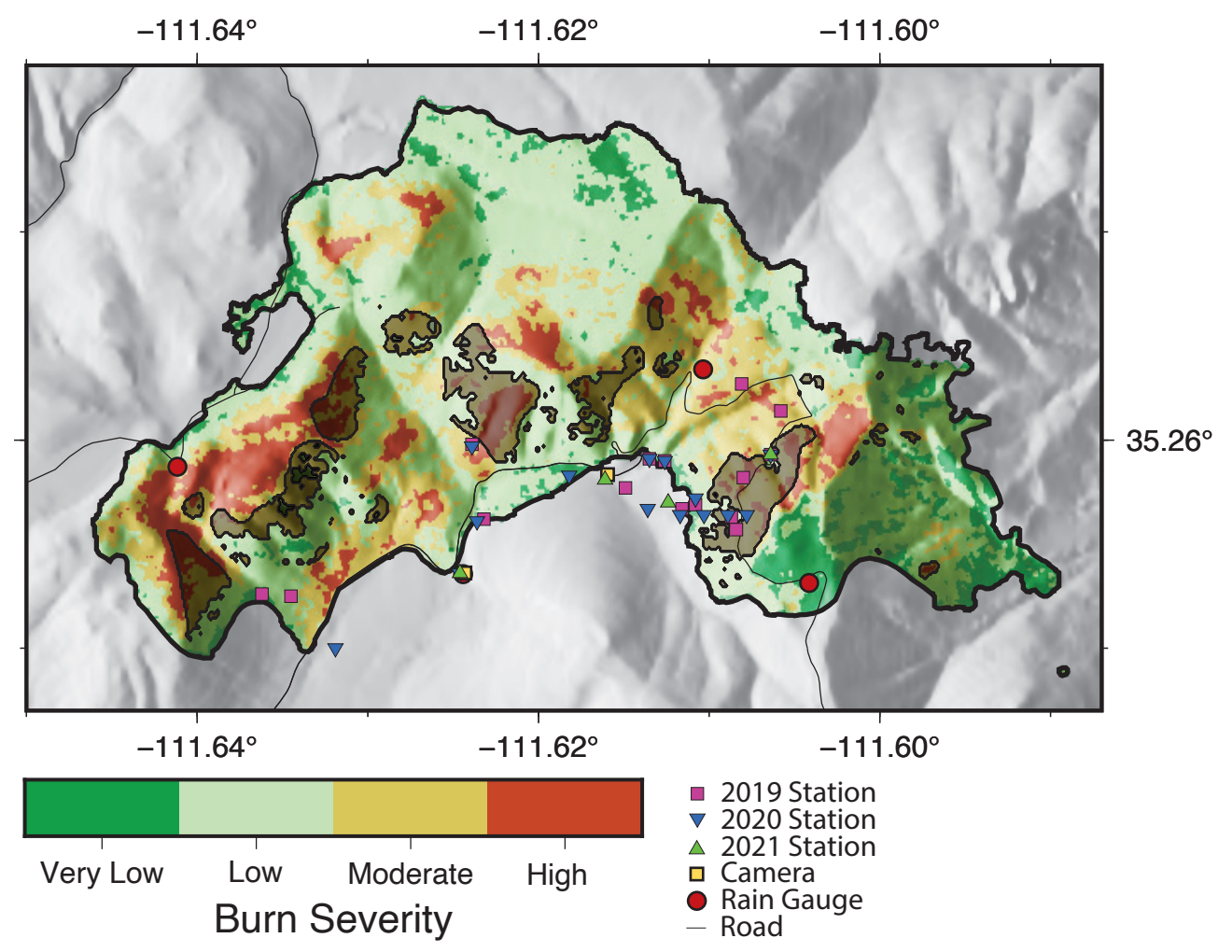
−111.64°
−111.62°
−111.60°
35.26°
Very Low
Low
Moderate
High
Burn Severity
2019 Station
2020 Station
2021 Station
Camera
Rain Gauge
Road

Figure 3.

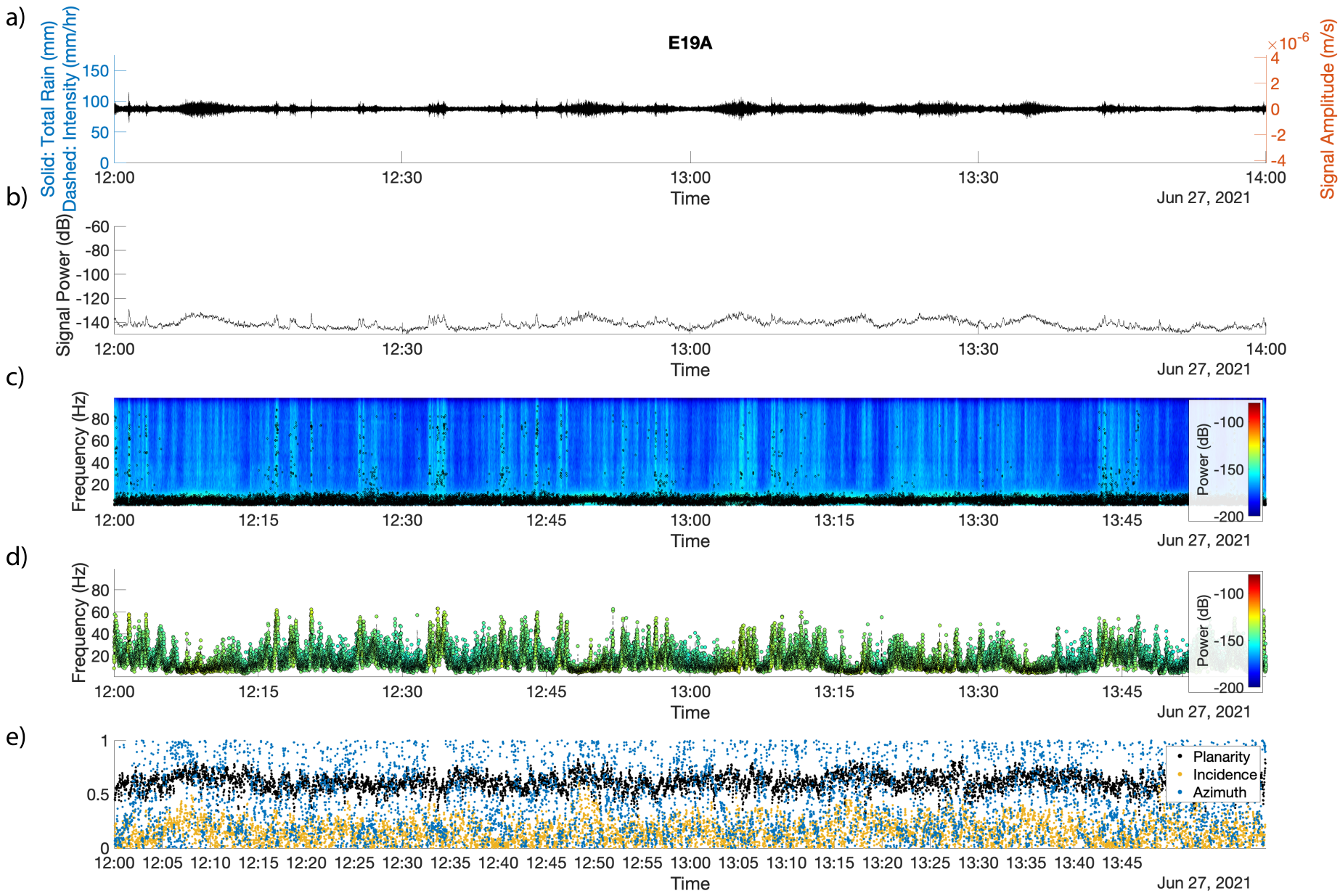
a)
E19A
Solid: Total Rain (mm)
Dashed: Intensity (mm/hr)
Signal Amplitude (m/s)
×10^-6
150
100
50
0
4
2
0
-2
-4
12:00
12:30
13:00
13:30
14:00
Time
Jun 27, 2021
b)
Signal Power (dB)
-60
-80
-100
-120
-140
c)
Frequency (Hz)
80
60
40
20
Power (dB)
-100
-150
-200
d)
e)
1
0.5
0
Planarity
Incidence
Azimuth
12:00 12:05 12:10 12:15 12:20 12:25 12:30 12:35 12:40 12:45 12:50 12:55 13:00 13:05 13:10 13:15 13:20 13:25 13:30 13:35 13:40 13:45

Figure 4.

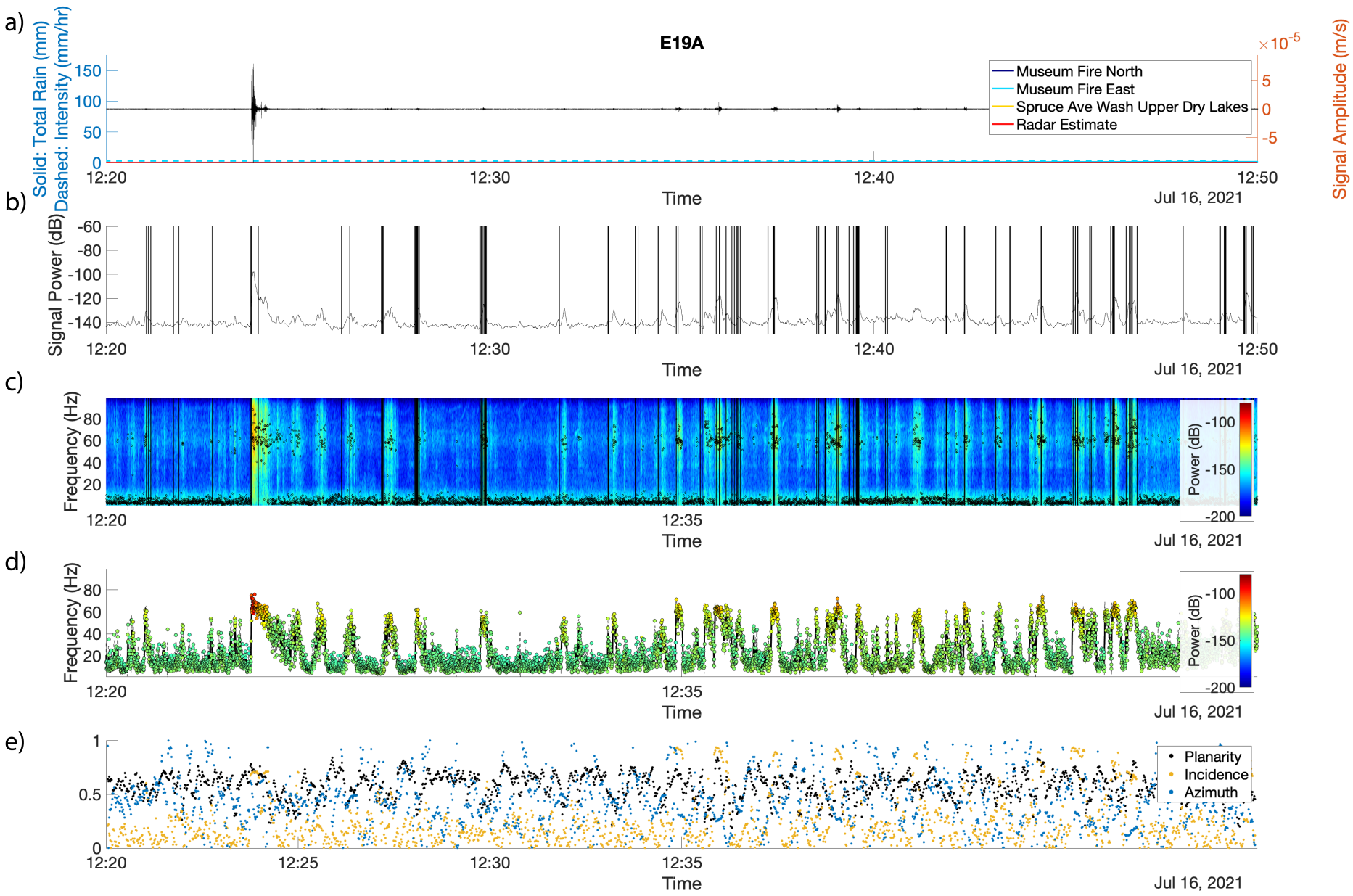
a)
E19A
Solid: Total Rain (mm)
Dashed: Intensity (mm/hr)
150
100
50
0
×10^-5
5
0
-5
Signal Amplitude (m/s)
Museum Fire North
Museum Fire East
Spruce Ave Wash Upper Dry Lakes
Radar Estimate
12:20
12:30
12:40
12:50
Time
Jul 16, 2021
b)
Signal Power (dB)
-60
-80
-100
-120
-140
12:20
12:30
12:40
12:50
Time
Jul 16, 2021
c)
Frequency (Hz)
80
60
40
20
Power (dB)
-100
-150
-200
12:20
12:35
Time
Jul 16, 2021
d)
Frequency (Hz)
80
60
40
20
Power (dB)
-100
-150
-200
12:20
12:35
Time
Jul 16, 2021
e)
1
0.5
0
Planarity
Incidence
Azimuth
12:20
12:25
12:30
12:35
Time
Jul 16, 2021

Figure 5.

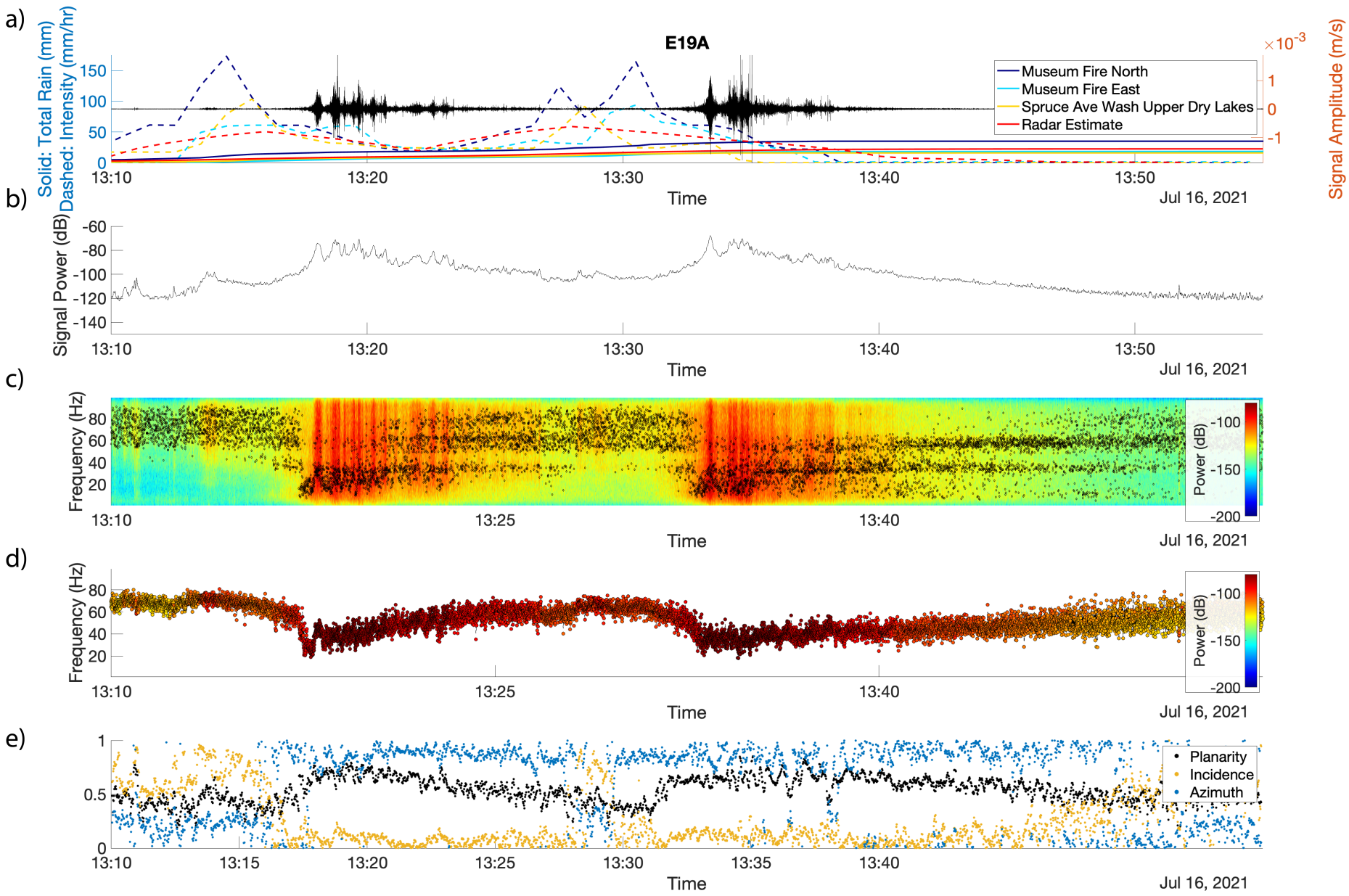
a)
E19A
Solid: Total Rain (mm)
Dashed: Intensity (mm/hr)
Signal Amplitude (m/s)
×10^-3
Museum Fire North
Museum Fire East
Spruce Ave Wash Upper Dry Lakes
Radar Estimate
Time
Jul 16, 2021
b)
Signal Power (dB)
c)
Frequency (Hz)
Power (dB)
d)
e)
Planarity
Incidence
Azimuth

Figure 6.

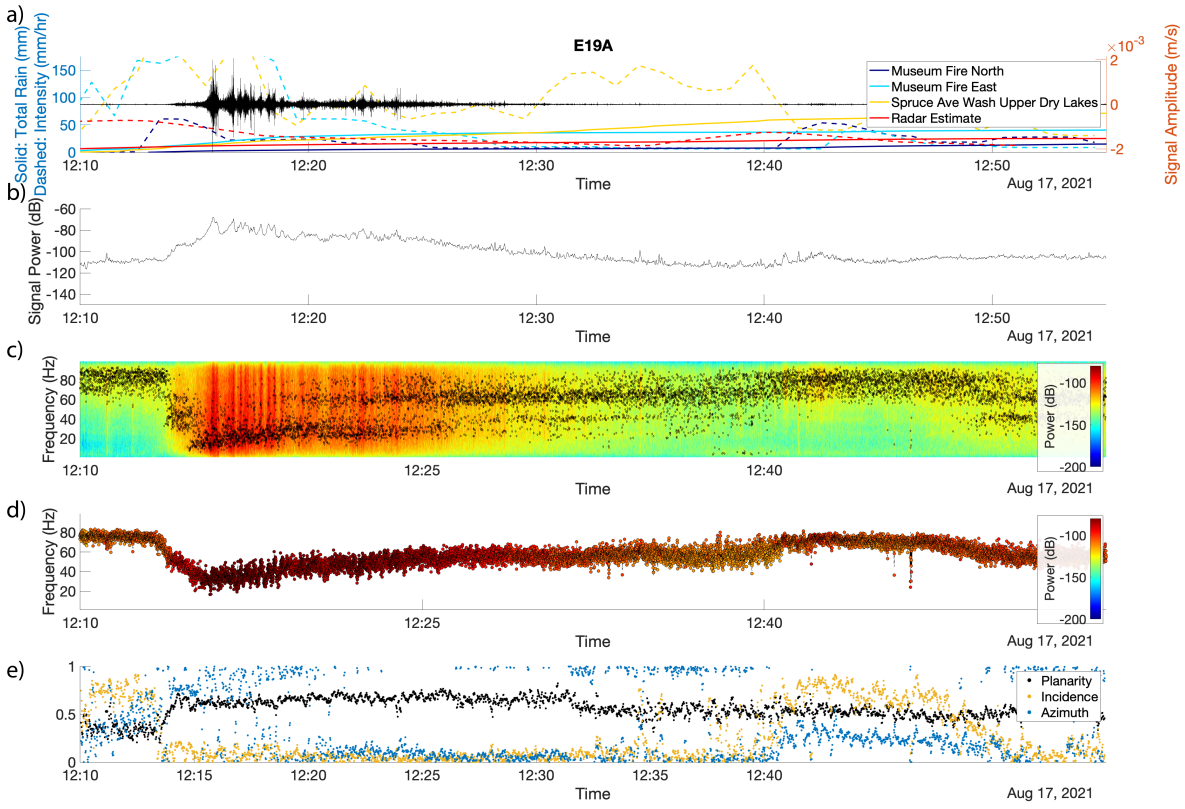
a)
E19A
Solid: Total Rain (mm)
Dashed: Intensity (mm/hr)
Signal Amplitude (m/s)
Museum Fire North
Museum Fire East
Spruce Ave Wash Upper Dry Lakes
Radar Estimate
Time
Aug 17, 2021
b)
Signal Power (dB)
c)
Frequency (Hz)
Power (dB)
d)
e)
Planarity
Incidence
Azimuth

f)


22.50 inHg - 71°F 08/17/2021 12:14PM CAMERA1

g)


22.50 inHg - 68°F 08/17/2021 12:19PM CAMERA1

Figure 7.

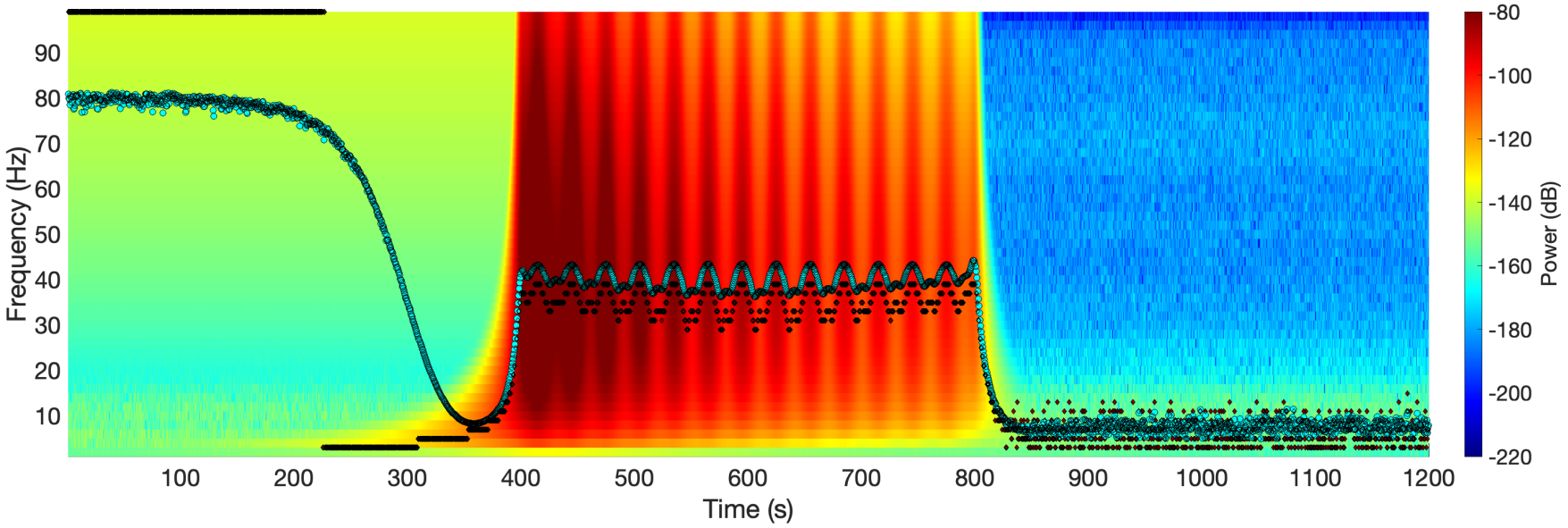
Frequency (Hz)
90
80
70
60
50
40
30
20
10
100
200
300
400
500
600
700
800
900
1000
1100
1200
Time (s)
-80
-100
-120
-140
-160
-180
-200
-220
Power (dB)

Figure 8.

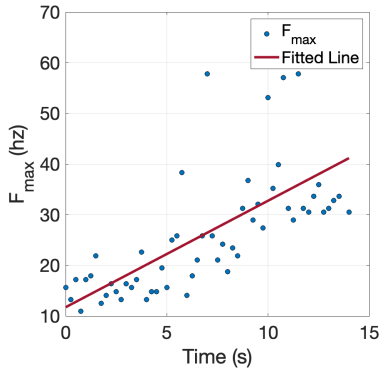
F max
Fitted Line
70
60
50
40
30
20
10
0
5
10
15
F max (hz)
Time (s)

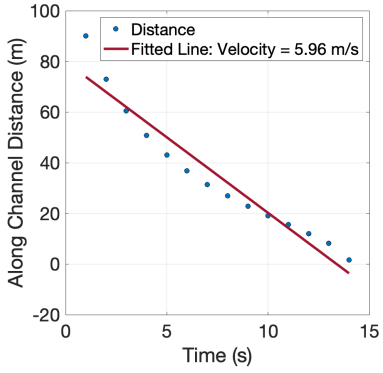
Distance
Fitted Line: Velocity = 5.96 m/s
100
80
60
40
20
0
-20
0
5
10
15
Along Channel Distance (m)
Time (s)

Figure 9.

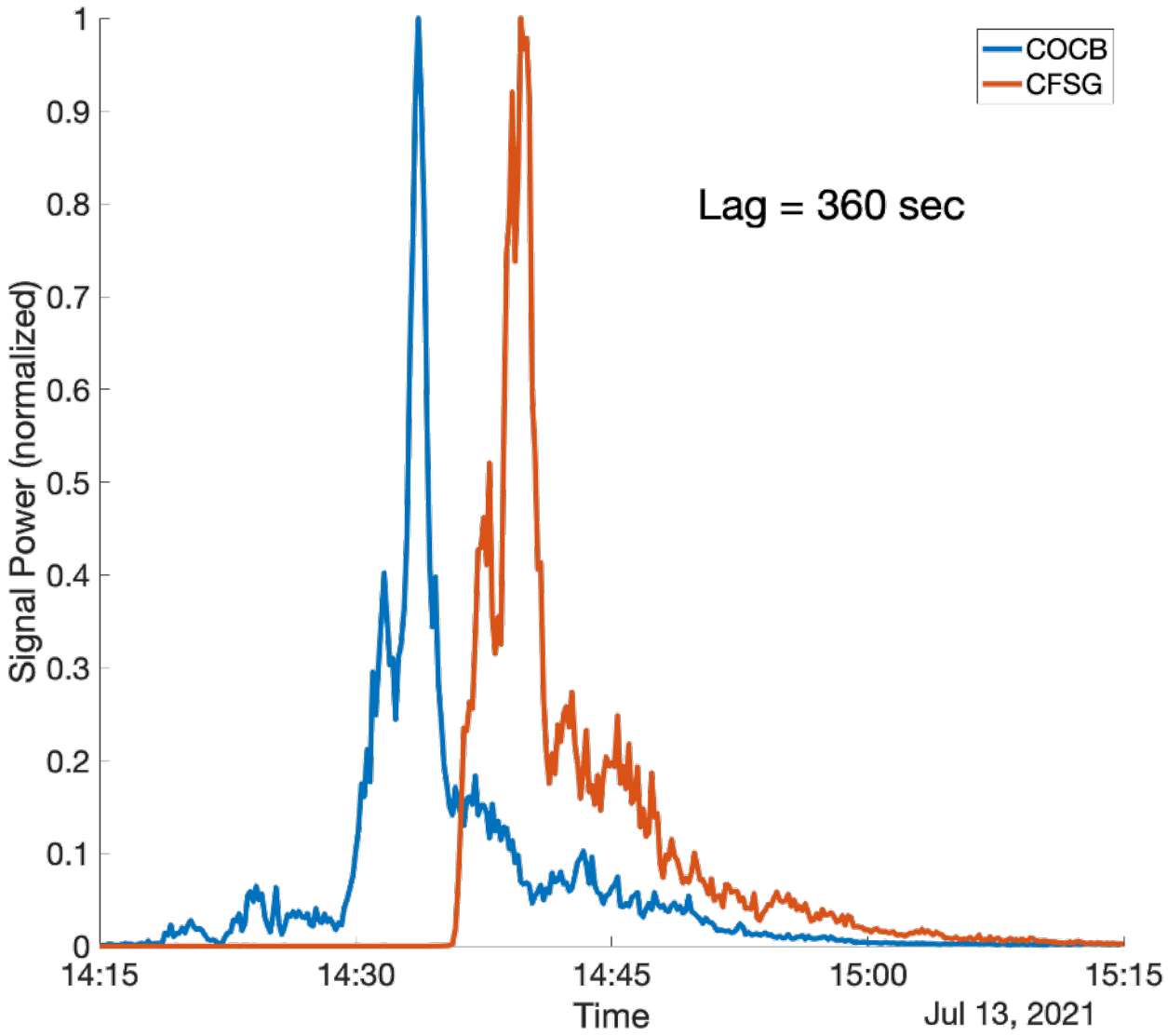
COCB
CFSG
Lag = 360 sec
Signal Power (normalized)
1
0.9
0.8
0.7
0.6
0.5
0.4
0.3
0.2
0.1
0
14:15
14:30
14:45
15:00
15:15
Time
Jul 13, 2021

Approximate Start Time	Approximate Duration (hr:min:sec)	Museum Fire West Peak 15-min Intensity (mm/hr)	Museum Fire West Peak 60 min Intensity (mm/hr)	Museum Fire West Storm Total (mm)	Museum Fire North Peak 15 min Intensity (mm/hr)	Museum Fire North Peak 60 min Intensity (mm/hr)	Museum Fire North Storm Total (mm)	Museum Fire East Peak 15 min Intensity (mm/hr)	Museum Fire East Peak 60 min Intensity (mm/hr)	Museum Fire East Storm Total (mm)	Spruce Ave Wash Peak 15 min Intensity (mm/hr)	Spruce Ave Wash Peak 60 min Intensity (mm/hr)	Spruce Ave Wash Storm Total (mm)
23-Jul-2019 15:50:00	00:15:03	N/A	N/A	N/A	N/A	N/A	N/A	N/A	N/A	N/A	45.45	13.66	11.68
28-Aug-2019 13:26:00	01:10:30	17.12	5.14	5.15	12.20	5.85	5.88	27.96	22.33	24.82	36.11	20.11	20.20
24-Jul-2020 14:36:00	00:59:29	18.07	9.25	9.25	49.19	17.85	17.85	24.09	12.01	12.00	29.02	10.99	10.99
30-Jun-2021 14:36:00	00:14:13	6.57	4.83	1.55	13.28	6.86	3.32	24.45	12.20	6.11	36.78	13.97	9.19
13-Jul-2021 14:16:00	01:06:46	81.28	39.12	39.13	105.06	44.46	45.26	63.80	24.85	25.05	29.72	20.51	21.03
14-Jul-2021 13:19:00	01:30:42	33.80	12.82	13.14	37.74	15.41	15.99	39.75	16.16	16.25	72.86	25.80	26.15
16-Jul-2021 12:32:00	01:21:59	50.48	18.17	18.17	63.33	35.08	35.09	40.71	19.85	20.54	38.40	16.24	16.30
21-Jul-2021 12:16:00	00:59:05	62.31	31.01	31.01	1.39	1.02	0.38	0.00	0.00	0.00	23.93	11.08	11.08
25-Jul-2021 16:00:00	00:21:22	35.36	9.34	9.22	25.24	7.16	6.43	16.64	4.98	4.32	55.90	13.97	13.97
17-Aug-2021 12:04:00	01:20:15	116.68	60.92	61.10	28.88	18.77	20.75	120.83	41.34	44.96	113.79	77.39	81.22

*Storm totals in mm; Intensities in mm/hr